Annals of Biomedical Engineering, Vol. 35, No. 11, November 2007 (© 2007) pp. 1840–1856
DOI: 10.1007/s10439-007-9356-0

Progress in the CFD Modeling of Flow Instabilities in Anatomical Total Cavopulmonary Connections

CHANG WANG,[1] KEREM PEKKAN,[1,2] DIANE DE ZÉLICOURT,[1] MARC HORNER,[3] AJAY PARIHAR,[4] ASHISH KULKARNI,[4] and AJIT P. YOGANATHAN[1]

[1]Wallace H. Coulter School of Biomedical Engineering, Georgia Institute of Technology, Room 2119 U. A. Whitaker Building, 313 Ferst Dr, Atlanta, GA 30332-0535, USA; [2]Department of Biomedical Engineering, Carnegie Mellon University, Pittsburgh, PA, USA; [3]ANSYS Inc., Evanston, IL, USA; and [4]Fluent India Pvt Ltd, Pune, India

(Received 21 May 2006; accepted 6 July 2007; published online 20 July 2007)

Abstract—Intrinsic flow instability has recently been reported in the blood flow pathways of the surgically created total-cavopulmonary connection. Besides its contribution to the hydrodynamic power loss and hepatic blood mixing, this flow unsteadiness causes enormous challenges in its computational fluid dynamics (CFD) modeling. This paper investigates the applicability of hybrid unstructured meshing and solver options of a commercially available CFD package (FLUENT, ANSYS Inc., NH) to model such complex flows. Two patient-specific anatomies with radically different transient flow dynamics are studied both numerically and experimentally (via unsteady particle image velocimetry and flow visualization). A new unstructured hybrid mesh layout consisting of an internal core of hexahedral elements surrounded by transition layers of tetrahedral elements is employed to mesh the flow domain. The numerical simulations are carried out using the parallelized second-order accurate upwind scheme of FLUENT. The numerical validation is conducted in two stages: first, by comparing the overall flow structures and velocity magnitudes of the numerical and experimental flow fields, and then by comparing the spectral content at different points in the connection. The numerical approach showed good quantitative agreement with experiment, and total simulation time was well within a clinically relevant time-scale of our surgical planning application. It also further establishes the ability to conduct accurate numerical simulations using hybrid unstructured meshes, a format that is attractive if one ever wants to pursue automated flow analysis in a large number of complex (patient-specific) geometries.

Keywords—Fontan operation, Digital particle image velocimetry (DPIV), Flow instability, Computational Fluid Dynamics (CFD), Patient specific, Surgical planning, Total Cavopulmonary Connection (TCPC).

Address correspondence to Ajit P. Yoganathan, Wallace H. Coulter School of Biomedical Engineering, Georgia Institute of Technology, Room 2119 U. A. Whitaker Building, 313 Ferst Dr, Atlanta, GA 30332-0535, USA. Electronic mail: ajit.yoganathan@bme.gatech.edu

INTRODUCTION

The Total Cavopulmonary Connection (TCPC) is the preferred procedure for surgical repair of single ventricle heart disease. This surgical procedure involves the anastomosis of the inferior vena cava (IVC) and superior vena cava (SVC) to the pulmonary arteries (PA) such that the right side of the heart is bypassed to prevent the pathological condition due to the mixing of oxygenated and deoxygenated blood inside the heart.[16] The resultant TCPC morphologies, however, introduce non-physiologic complexities for the blood flow. *In vitro* experimental studies[15,23] as well as previous computations[7,15] have shown that given a steady inflow condition with flow rates within the laminar regime, highly unsteady vortical motion is persistently created within the connection region. The unsteadiness manifests itself in the form of seemingly chaotic meandering of the flow recirculation into PA and venae cavae. The onset of this complex three-dimensional (3D) flow is a consequence of non-linear 3D flow instabilities generating small-scale perturbations at the stagnation region where the SVC and IVC flows collide. This highly disturbed flow pattern is characterized by regions with high velocity gradients and is therefore very dissipative. An accurate prediction of the detailed transient flow evolution is critical to the evaluation of the energy loss within the connection, which is the primary variable for evaluating the efficiency and consequently optimizing the TCPC design.[10] Recent lumped parameter modeling studies[21] have shown that venous power loss has a significant impact on cardiac output and venous blood volume share in single-ventricle circulation. Advances in fluid flow modeling of complex TCPC anatomies is even more critical as new virtual patient-specific surgical planning tools are introduced[28] and proven to be potentially useful in several clinical cases.[22,32] Accurate

modeling of the unsteady flow deserves added emphasis as the right-heart bypass and diaphragm movement introduces significant unsteadiness to the otherwise steady single-ventricle venous flow.

A recent numerical study of realistic TCPC anatomy using the commercially available computational fluid dynamics (CFD) tool FIDAP (ANSYS Inc., NH) successfully captured the global, time-averaged features of the experimental flow fields using a first-order upwinding scheme.[23] However, the overly dissipative nature of the low-order led to a loss of dynamic information in the Navier–Stokes equations. Attempts to run FIDAP in transient mode with 4-node unstructured tetrahedral finite-element grids and second-order discretization were inconclusive using practical time steps and mesh resolution. It is acknowledged in the CFD community that attempts at simulating complex 3D highly unsteady flows using most prevalent commercial flow solvers will fail to obtain convincing results with the default solver parameters and unstructured grids.[24,30] This position stems from the experience gained in simpler benchmark geometries[2,13] which were chosen because of their ability to test one or more key modeling objective but do not properly represent the geometrical complexity encountered in *in vivo* configurations, thus emphasizing the need for CFD studies in anatomically accurate geometries.

An additional crucial issue when considering biomedical applications is the large sample size required in order to draw any statistically significant conclusions. Cebral *et al*. studied cerebral aneurisms in 62 patient-specific models.[5] For our topic of interest, the TCPC, the sample size requirements is of 10 cases per major template in order to discern the different surgical designs[6,27] which leads us to a minimum of 50 test-cases for a thorough patient-specific study. Conducting such studies and further down the line, applying them to patient-specific pre-surgical planning requires high-performance clinical computer clusters and an efficient model generation pipeline.[4] Few studies have reported on the efficacy and feasibility of parallel simulations for patient-specific modeling. Dong and coworkers have successfully distributed one large-scale patient-specific model to multiple long-distance international clusters through the TeraGrid consorsium.[9] Fisher *et al*. presented parallel performance and scalability for a patient-specific carotid artery model using up to 1024 processors in the Pittsburgh Supercomputing Center.[12] However, these studies used computational resources that are beyond the realm of any clinicians and very little attention has been given to the parallel CFD performance of cardiovascular anatomical models in dedicated single-user moderate computer clusters which are more clinically accessible at the present time. To the best of our knowledge, only Yue *et al*.[29] reported the parallel performance and scalability (of a carotid artery test case) in easily accessible Linux clusters with up to 16 processors. They showed that the scale-up was linear up to that point.

The study presented here explores the accuracy and parallel performance of a commercial CFD package, FLUENT (ANSYS Inc, NH) using a second-order upwind scheme based on finite-volume discretization. The higher-order discretization is considered to be more suitable when computing inherently unsteady flow. This study will focus on assessing the accuracy with which FLUENT predicts unsteady unstable laminar flows in two arbitrarily complex, patient-specific TCPC anatomies: models A and B as shown in Figs. 1a and 1b. Model A, which exhibited the most unsteadiness, was retained to validate the simulation results. First, computational flow fields and velocity magnitudes are compared with the experimental, unsteady, 2D particle image velocimetry (PIV) measurements. We then compare the spectral content and unsteady intensity of the numerical and laboratory flows. It should be emphasized that the observed unsteadiness in our study emerged naturally as a result of instability within the connection itself and without any explicit forcing, such as an input flow wave form.

In the literature, the intrinsic flow instability of the TCPC is reported only for a single anatomical model, which was an intra-atrial TCPC[23] (the same as Model A). Consequently, it is still uncertain whether the observed flow instability is a characteristic of all TCPC templates. To augment our understanding, and as a continuation of the previous work, this study also reports the unsteady flow characteristics of a typical extra-cardiac baffle IVC-to-MPA TCPC (Model B), featuring more uniform blood flow pathways compared to the intra-atrial type (Model A). Transient computations on Model B were run for two cardiac outputs (3 and 4 L/min) and five pulmonary flow splits (going from 30/70 to 70/30 LPA/RPA by 10% increments) underscoring the impact of the hemodynamic operating points on the observed flow oscillations and vortical structures.

METHODOLOGY

This study features two TCPC morphologies: Model A (Fig. 1a), which is an intra-atrial connection, and Model B (Fig. 1b), which is an extra-cardiac IVC-to-MPA connection. Both geometries were obtained from magnetic resonance images (MRI) of the patients' thorax. The surface of the TCPC blood volume was reconstructed from the MRI data using an in-house code and used to generate both the numerical mesh

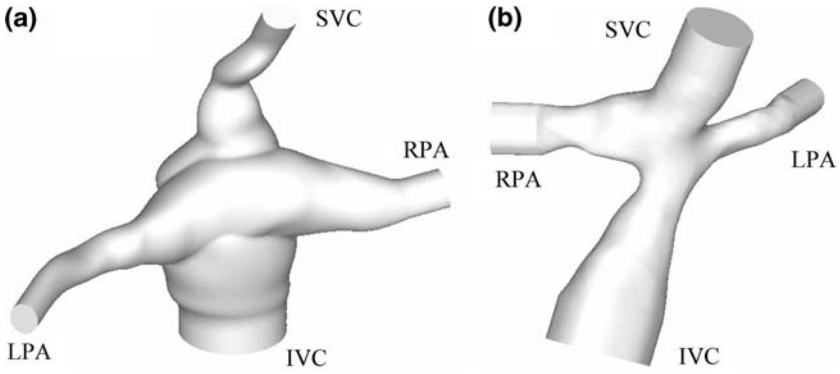

FIGURE 1. Geometries of the two TCPC anatomies retained for this study: (a) Model A and (b) Model B.

and the physical model used in the *in vitro* experiments. The *in vitro* model was manufactured by stereolithography using an SLA® 250 (3D Systems, Valencia, CA) system, with Renshape 5510 transparent resin (Vantico AG, Basle, Switzerland) and a build accuracy of 0.004 in. (0.1 mm).[31]

The major advantage of this approach, which is described in further details by Zélicourt and associates,[31] was that it allowed for identical numerical and experimental geometries, which was crucial for this study. The remaining of this section describes the details of the computational and experimental work.

Mesh Generation

The CFD grids were generated using GAMBIT (ANSYS Inc, NH) version 2.1.2 on a Linux platform. A brief overview of the mesh characteristics for Models A and B can be found in Table 1, while the following paragraphs summarize the steps followed during the mesh generation process are outlined below, using model A as an example:

1. Import the IGES surface patch file that defines the anatomy to the mesh generator. The imported model contained a number of small surface zones, called patches. Small patches were merged to form several large faces using the virtual face merge tool. These faces are stitched together defining the 3D volume of the TCPC anatomy.
2. The resulting surface was meshed using a Tri/Pave scheme with an interval size of ~0.3 mm defined at boundary edges as shown in Fig. 2a.
3. As compared to tetrahedral cells, prismatic elements are recommended for improving accuracy near the walls. The surface triangles were extruded in the direction normal to the wall (a mapped mesh) to create a smooth boundary layer zone. The growth factor when going from one row to the next was set to one in this case, therefore the height of each element is constant in the boundary layer, see Fig. 2b. The boundary layer was five elements thick.
4. It is always advisable to use hexahedral (hex) elements for improved numerical accuracy and computational efficiency (See Baran[1] for a recent review). A "Hex-Core" meshing strategy was utilized which consisted of unstructured hexahedral cells in the central region of the volume, surrounded by a few layers of tetrahedral cells. The tetrahedral cells provide a smooth transition to the prismatic boundary layer mesh on the wall. This methodology is practical when generating quality meshes with complicated boundary structures that would be difficult to mesh otherwise, it is also readily automated. The results of using this procedure for Model A are illustrated Fig. 2c. Note that the final mesh contained three types of elements: hex in the center, tetrahedral cells surrounding the hex elements and prisms along the wall, see Fig. 2d.
5. The inlets and outlets were extended to minimize the effect of entrance and exit boundary conditions on the flow patterns in the actual anatomical domain. In our study, each inlet/outlet face was normally swept 5–10 times the vessel diameter. The Hex/Cooper scheme was used to generate a pure hex mesh in the extended regions.

TABLE 1. Time-step and mesh resolution used in the simulations.

Model	Time step (s)	Average grid size (mm^3)	Node number	Element number
A	0.002	6.29e-2	288,805	679,648
B	0.005	2.49e-2	110,421	552,200

The time steps reported here correspond to the largest time-step used. Smaller time-steps are used for the first iterations and gradually increased through a series of load step blocks.

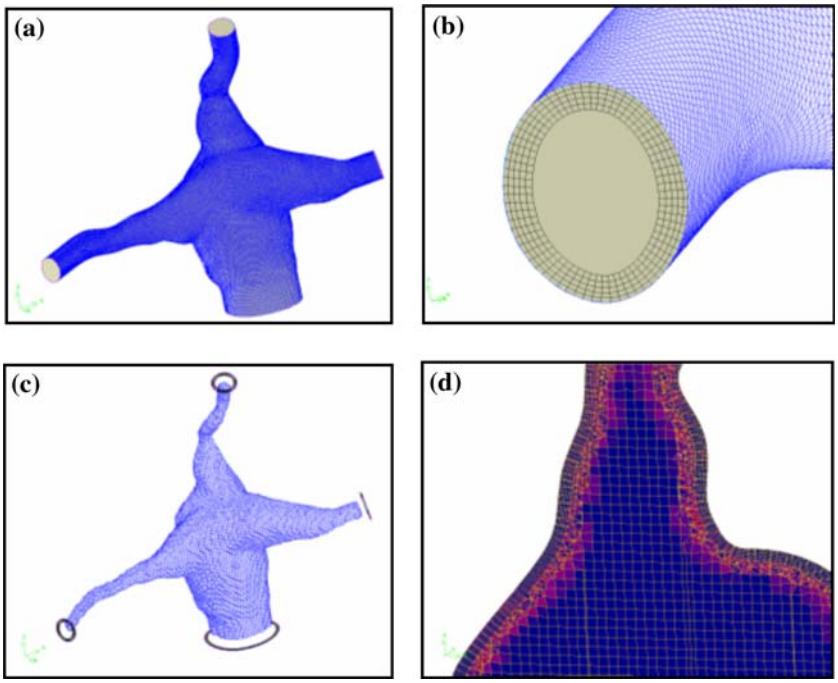

FIGURE 2. Hex-Core Mesh Architecture. (a) Triangular surface mesh; (b) Uniform tetrahedral mesh representing the boundary zone; (c) Uniform hexahedral mesh used at the model core; (d) Typical tetrahedral interface zone connecting uniform tetrahedral elements to hexahedral cubes.

Numerics

Material Properties and Boundary Conditions

Blood was assumed incompressible and Newtonian, which is consistent with previous experimental and numerical studies ($\rho = 1060$ kg m^{-3}, $\mu = 3.5 \times 10^{-3}$ Pa s). The vessel surfaces were treated as rigid and impermeable walls. A 40/60 SVC/IVC mass flow rate ratio was specified as inflow conditions. We tested two types of FLUENT outflow boundary conditions in this study, namely the pressure-outlet condition—which is a non-reflecting boundary condition where a pressure value is specified at each outflow—and the mass flow split—where the velocity values are extrapolated from the upstream nodes and adjusted by a scaling factor to obtain the same mass flux split ratio as used in the experiments. To apply the pressure-outlet condition, the pressure values are given at PA outlets depending on the expected flow split between two PAs using pressure difference vs. flow rate correlation obtained from previous auxiliary CFD runs using FIDAP.[23] The flow splits specified above may be entered directly when using the mass flow split condition. Theoretically, pressure boundary conditions should be more consistent with flow physics since fluctuations of the pressure field are typically lower in magnitude than fluctuations in velocity field (which directly determines the flow rate). However, the tests conducted for Model A did not demonstrate any significant difference in the flow fields obtained with either type of outflow conditions. The same observation was confirmed in Model B. The major advantage of the pressure outflow condition was that it resulted in faster convergence rates than the flow-split boundary condition, but this approach was still not practical as it required auxiliary runs to establish the relation between flow-split and outflow pressure conditions.[23] All the computations in the present study were therefore conducted by specifying the mass flow split (Table 2).

A fully developed velocity profile was applied at the inlets from the SVC and IVC to match experimental flow conditions. Owing to the non-circular shape of these inlets, the velocity profiles were obtained numerically using the SVC and IVC cross-sectional shapes as the starting point. These cross-sections were

TABLE 2. Correspondence between the mass flow boundary conditions and overall pressure drops for two sample flow conditions in Model A and Model B.

Model	IVC (L/min)	SVC (L/min)	LPA (L/min)	RPA (L/min)	ΔP* (mmHg)
A (1 L/min)	0.6	0.4	0.5	0.5	–2.88
B (4 L/min)	2.4	1.6	2.8	1.2	–4.97

The pressure drop given in last column $\Delta P = \frac{1}{2}(P_{LPA} + P_{RPA}) - \frac{1}{2}(P_{IVC} + P_{SVC})$ represents the equivalent pressure drop through the TCPC between venous to pulmonary pathway. Typical venous pressures for single ventricle patients are in the order of 15 mmHg measured with respect to atmosphere.

extended ~50 diameters in the normal direction. The material properties and flow rates were set as described above and then solved using a plug-flow inlet boundary condition. The x-velocity, y-velocity and z-velocity of the outflow of these pipe models were written as profile files and subsequently used to specify the fully developed inflow profiles at SVC and IVC in the corresponding TCPC simulation.

For all simulations, we first obtained the steady solution and then used it as initial condition for the subsequent transient computation. This procedure allowed for a faster temporal convergence. We employed a variable time-stepping scheme, which adjusts the time-step based on a prescribed Courant number and the velocity magnitude at the previous iteration with no user intervention. This improves transient efficiency and robustness, particularly in cases where the velocity changes significantly with time. The convergence criterion was set to 10E-5 for all degrees-of-freedom.

Solver Settings

The beta version of FLUENT 6.2.5 was used for the numerical simulations. The FLUENT segregated solver was applied to solve the continuity equation and the linearized momentum equations sequentially. The convection terms in the momentum equations were discretized using a second-order upwinding scheme. Considering the transient nature of the problem and the possibility of high degree of mesh skewness (during routine use of this model), the pressure–velocity coupling algorithm was chosen to be PISO (Pressure-Implicit with Splitting of Operators) to improve the convergence rate. FLUENT uses a co-located scheme and both velocity and pressure values are stored at cell centers. To account for the curved TCPC anatomical geometry and the presence of rotational flow structures, the PRESTO (Pressure Staggering Option) method was selected in this study as the pressure interpolation procedure to obtain the pressure values at cell faces for the discretization of momentum equations. The second-order implicit scheme was used to integrate the solution in time.

Computer Cluster and Parallel Considerations

All computations were performed on a Beowulf computer cluster. The computer nodes were connected via a state-of-the-art Myrinet high-speed network with low latency. Each node has two 1.6 GHz 64 bit AMD Opteron 242 processors with 2.0 GB RAM. The cluster was tested using the standard NASA Advanced Supercomputing Division parallel benchmarks (NPB), indicating a high-level of parallelization efficiency. Furthermore, to document the actual parallel performance, the unstructured grid of Model A was partitioned and the computation was distributed between to 36 parallel nodes using the Message Passing Interface (MPI) based distributed memory computing technologies. Snapshots of the partitioned mesh for Model A are illustrated in Fig. 3. For this model the parallelization performance of FLUENT is given in Fig. 4. The efficiency dropped substantially beyond 16 processors (before that the speed-up is super-linear), which is believed to be due to the fact that the built-in automatic partition algorithm of FLUENT does not necessarily provide the most optimized decomposition of complex computation geometry (As the manual decomposition has not been tried due to the complexity of the anatomic geometry, this hypothesis was not tested). Computations typically took about 30 h wall time to simulate a physical process of 20 s for unsteady TCPC flow in model A.

Digital Particle Image Velocimetry (DPIV)

Model A was also studied experimentally using DPIV. We used a TSI system (TSI Inc, Shoreview, MN), which included a data acquisition software package (Insight 3.34), two 17 mJ miniYag lasers (λ = 514 nm) and one camera. In order to increase image quality, fluorescent Rhodamine B particles

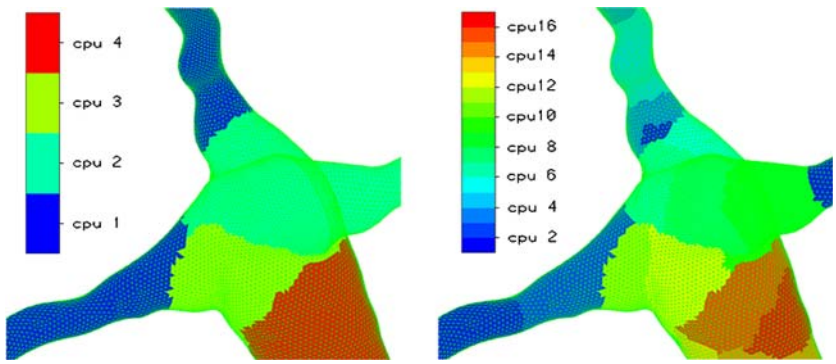

FIGURE 3. Sample partitioned meshes for Model A distributed to 4- (left) and 16-computer nodes (right).

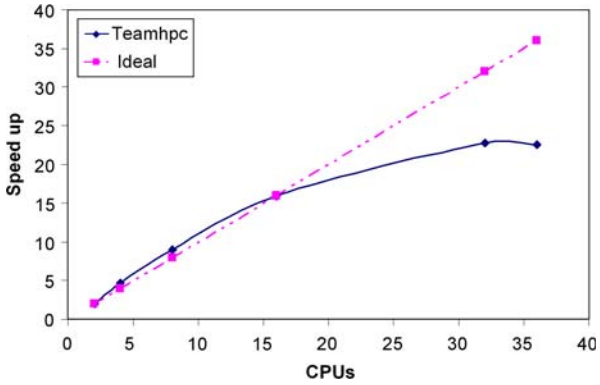

FIGURE 4. Parallel performance of FLUENT assessed for Model A on a Beowulf computer cluster.

(MF/RhB, size range: 2.5–5 μm, Microparticles GmbH, Berlin, Germany) were used to seed the flow. The emission spectra of Rhodamine B peaks around 590 nm, so that a red color filter (λ = 570 nm) was used to cut off the laser beam reflections on the model surfaces while still allowing the fluorescent particles to shine through. An aqueous solution of glycerin and sodium iodide was used to match both the kinematic viscosity of blood (μ = 3.5 cSt + 0.1 cSt) and the refractive index of the rapid prototyping resin (n = 1.51).

Velocity data were acquired in the coronal plane. About 300 double frames were acquired at each location at 15 Hz. The selection of 300 pairs was aimed at obtaining a representative mean field. As an accuracy check we processed the batch of data with different number of frames: 10, 50, 100, 150, 200, 250, and 300. The variation between the average obtained with 200 and 300 frames was $<5\%$, and the variation between 250 and 300 frames was less than 2.5%. It was thus considered that sufficient convergence of the running average was achieved with 300 frames. Moreover, when acquiring more than 300 double-frames (which could have been possible) storage of data becomes a serious issue; 300 was thus a balance between convergence and data storage space.

Cross-correlation vectors were computed with DaVis 6.2.2 (LaVision Gmbh, Gottingen, Germany). A mask was applied to filter out the region of interest. The vectors were computed using the Fast Fourier Transform in multiple passes, without zero padding. The interrogation window was progressively decreased (64×64 pixels down to 16×16 pixels) and a 50% overlap window was specified, satisfying the Nyquist condition. Intermediate flow fields were smoothed out, but no smoothing was applied after the last pass. The 300 instantaneous flow fields were averaged into a single frame.

RESULTS

Model A: Average Velocity Field

For the purpose of validation, we compared the time-averaged flow fields obtained from the transient computation to DPIV measurements and to previous first-order (steady-state) computations for Model A. Figure 5 shows the contour plots of in-plane velocity magnitude in four coronal slices, going from the most anterior (a) to the most posterior (d) positions. The time-averaged flow fields obtained with both FIDAP and FLUENT are in reasonable agreement with the generic flow patterns observed in the experiments. The flow features predicted by the current study are essentially similar to that reported in Pekkan *et al.*[23] and are thus not described in detail here. This comparison suggests that in terms of the accuracy in capturing the general flow structures, the present second-order accurate (in convective term discretization) transient simulation is comparable to previous numerical predictions with lower order accuracy.[23]

Further attention, however, should be directed to two interesting observations from this comparison. First, the low flow region in the center of the connection site predicted from the present study is relatively smaller in size than that from Pekkan *et al.*[23] The size of this low flow region as measured by DPIV lies between the two numerical simulations. As we know, the flow phenomenon in this area arises from the direct collision of SVC and IVC jets and is dominated by an intense flow recirculation structure throughout the pouch region. Based on our flow visualization experiments, the vortex motion persistently induces flows separated from SVC and IVC streams along left and right walls of the connection towards the collision site and thus squeezes the size of the stagnation region. In Figs. 5b and 5c, the trend of flow streams attached to the two sidewalls being spread into the interior connection area is clearly visible in the DPIV contour plot. These regions are marked as R1 and R2 in Fig. 5, where it can be observed that sizes of these regions are better predicted with the current second-order transient simulation than the first-order calculation shown in middle contour plot of Fig. 5c. The Region R2 appears as a localized spot in the first-order simulation while in PIV and in the second-order solution it is a larger complex flow region spreading from the pulmonary branch to IVC. Likewise, the size of region R1 in the second-order calculation is closer to the PIV measurements. These differences also translate into a better prediction of the flow streamlines with the present study. As shown in Figs. 5b and 5c FLUENT captures the major vortex core of the anatomy. To illustrate these improvements even further, flow

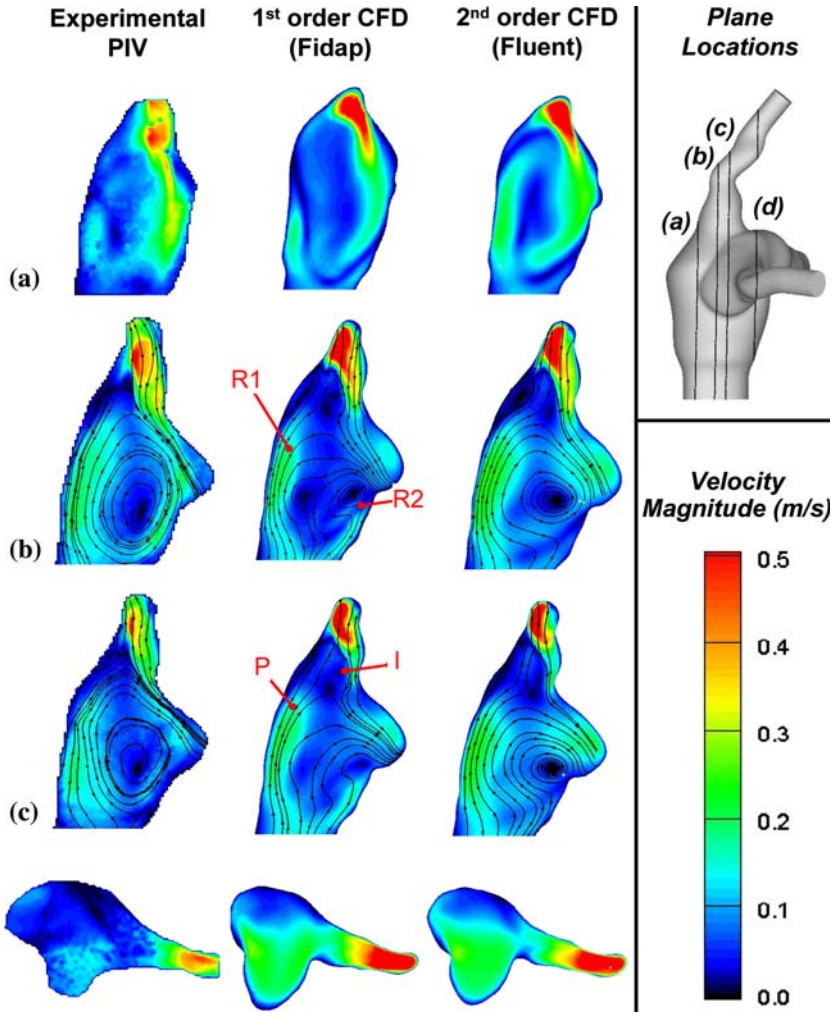

FIGURE 5. Quantitative assessment of the flow field of Model A using PIV, CFD 1st and 2nd order accurate. Flow conditions: total cardiac out put of 1 L/min; inflow split: 60/40 IVC/SVC; outflow split: 50/50 LPA/RPA. Imaged planes are indexed from the most anterior (a) to the most posterior (d). Slice locations are displayed on the upper-right diagram. For descriptions on flow regions R1 and R2 and points P and I refer to Sections "Model A: Average Velocity Field" and "Model A: Instantaneous Velocity Fields."

profiles obtained by the two codes and the PIV measurements are compared quantitatively in Fig. 6. These imply that the complex interaction between different flow regions (jet-like inflow and stagnant flow in the center of the connection) is only available from the second-order simulation. In this sense, the present predictions are believed to more correctly reflect the flow physics below the collision site. Secondly, as discussed in Pekkan *et al.*,[23] the experimental results reveal that the SVC inflow stream dives down into the lower area of the pouch region forming a continuous flow stream all the way along the left anterior wall.

Model A: Instantaneous Velocity Fields

Figures 7a–7c shows three pairs of representative snapshots of instantaneous velocity contour plots obtained in the unsteady DPIV measurements and in the current transient simulation, for a cardiac output of 3 L/min ($Re_{IVC} = 800$). The richness of unsteady flow dynamics is evidently recorded. This comparison shows a reasonable similarity between the instantaneous velocity fields and flow structures obtained experimentally and numerically at different stages of flow evolution. This suggests that the present flow solver used with the aforementioned settings is capable of qualitatively capturing the dynamic behavior of this laminar, but still chaotic, TCPC flow motion. Quantitative agreement between experimental and numerical time series is discussed in the following section.

Model A: Time Series and Frequency Content

A quantitative agreement of the transient flow evolution is demonstrated in Fig. 8, where the in-plane instantaneous velocity magnitudes are compared with

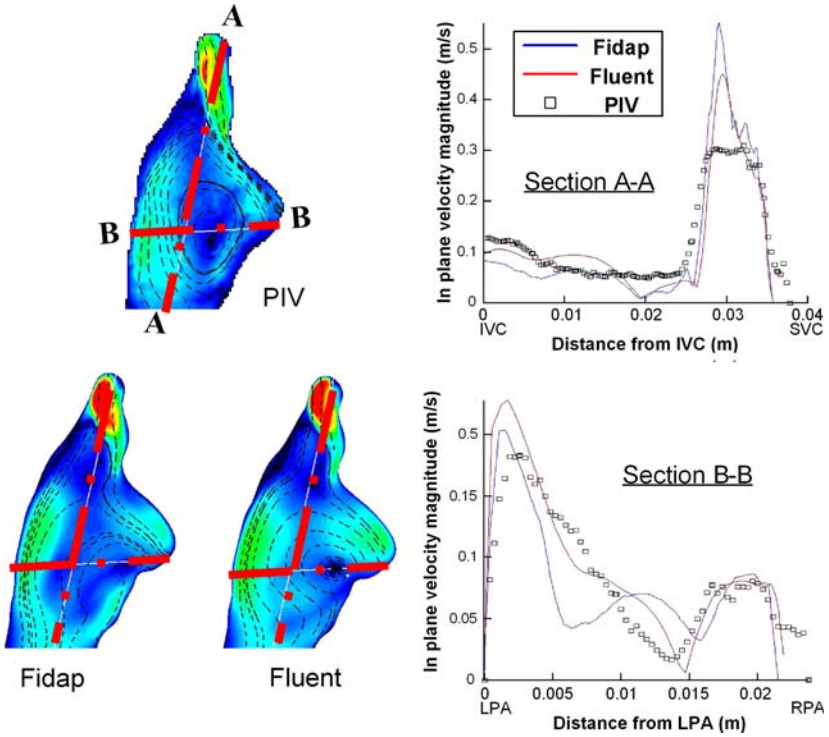

FIGURE 6. Comparison of the PIV and CFD in-plane velocity profiles for two cross-sections (A-A and B-B) taken in the sagittal plane shown in Fig. 5c.

the measurements sampled at 15 Hz at a point selected in the pouch region of Model A (point P in Fig. 5). The mean values and standard deviations were calculated to be 0.215 ± 6.254E-2 m s^{-1} and 0.182 ± 4.069E-2 m s^{-1} for computational calculations and experimental measurements, respectively at point P. The pouch region is defined to be the "power region" of this anatomy where intense mixing occurs. It is worth noting that this type of comparison is typically inaccurate by one or two orders of magnitude for most commercial codes.

Another interesting finding is obtained from the power spectrum of this time series. The experimental power spectrum (see Fig. 9) shows that most of the energy was contained in the lower frequencies, with two additional distinct peaks at 6.1 and 7.3 Hz. If the two higher frequency peaks were resolved with lower power in the CFD power spectrum, the rest of the dynamic frequency range displayed a trend that was similar to the experimental data. Specifically, the four peaks clustered between 0 and 1 Hz and the one at 2.3 Hz were well captured in the numerical simulations.

In general, the computations predicted richer frequency content as compared to the experiments, which may be attributed to the additional details of the finer scale flow structures and to periodic discretization errors. For this flow regime it has been observed that the unsteadiness is not continuous, but expressed as irregular pieces during the experiments. To illustrate this for Model A, the bottom plot in Fig. 9 displays the experimental and computational carpet plots of the aforementioned time series. These plots are color coded by power and display the energy content of a 10-s time-bin moving along the time series. Presenting the data in this way underscores the unsteady changes in the frequency content. The distribution of unsteady events was qualitatively similar for experiments and computations. In spite of the differences in the starting time of each data set almost all transient frequency peaks were captured correctly in relative locations.

Model B: Time-series and Frequency Content

The transient simulations conducted in Model B revealed a flow evolution that was much closer to being steady in time than in Model A. Flow oscillations were still observed but these seemed to have a coherent and almost periodic behavior in time. As shown in Fig. 10, the amplitude of the fluctuations was typically one order of magnitude lower than the mean velocity, where as mean velocity and velocity fluctuations were of the same order in Model A. This observation was in agreement with our flow visualization experiments which revealed very steady streaklines and "quiet" flow for Model B contrary to the chaotic flow behavior observed in Model A.

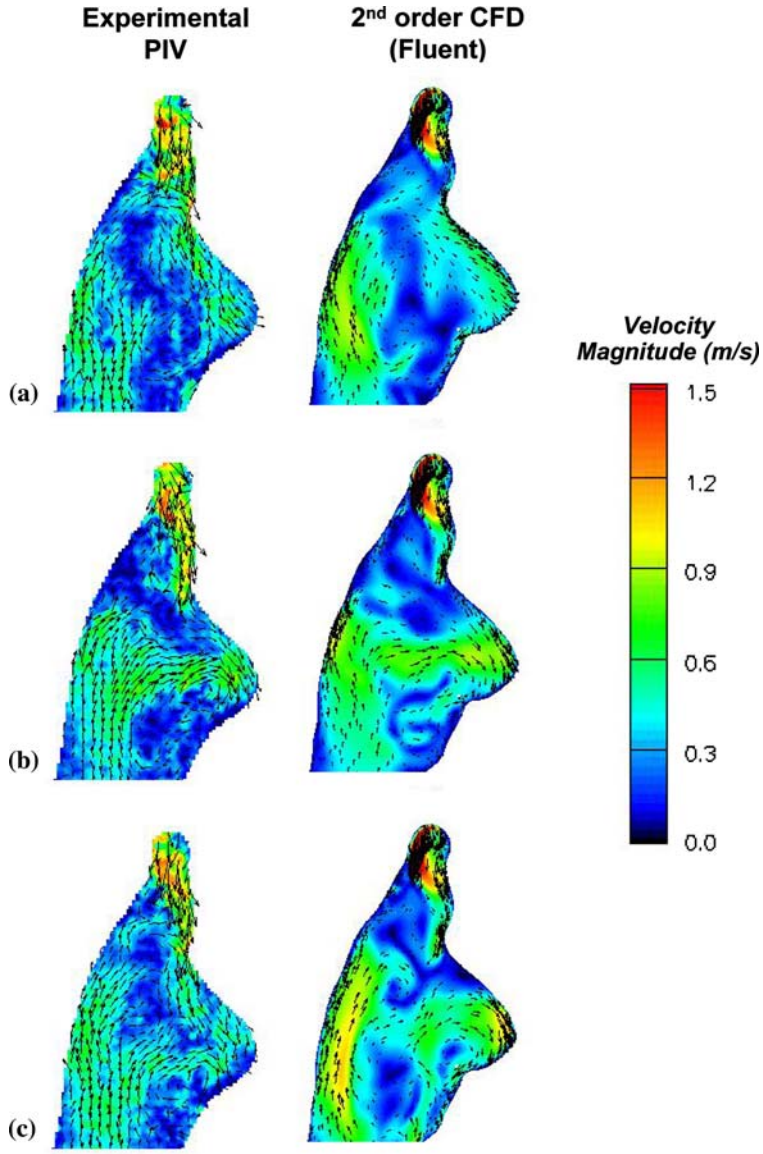

FIGURE 7. Quantitative assessment of the instantaneous flow field of Model A using PIV, 2nd order accurate at 3 L/min; inflow split: 60/40 IVC/SVC; outflow split: 50/50 LPA/RPA.

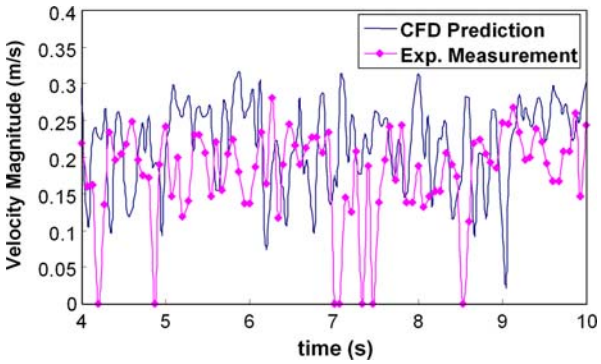

FIGURE 8. Instantaneous in-plane velocity time series at point P (see Fig. 5) in power region (pouch region) of model A. Experimental measurements were obtained at 15 Hz.

At all flow splits other than 70/30 LPA/RPA, a slow periodic oscillation was observed, with faster oscillations embedded within it. These faster oscillations contained most of the energy, and occurred at frequencies between 9 and 12.5 Hz depending on the total cardiac output and flow split. When more flow was forced through the RPA (at 30/70 and 40/60 LPA/RPA) the magnitude of the oscillations was larger than at 50/50 and 60/40 LPA/RPA flow splits, which translated into a much higher energy content of the dominant frequencies. A drastic change in overall behavior was observed at 70/30 LPA/RPA, when a large share of the flow was directed towards the smallest pulmonary artery, the LPA. The flow no

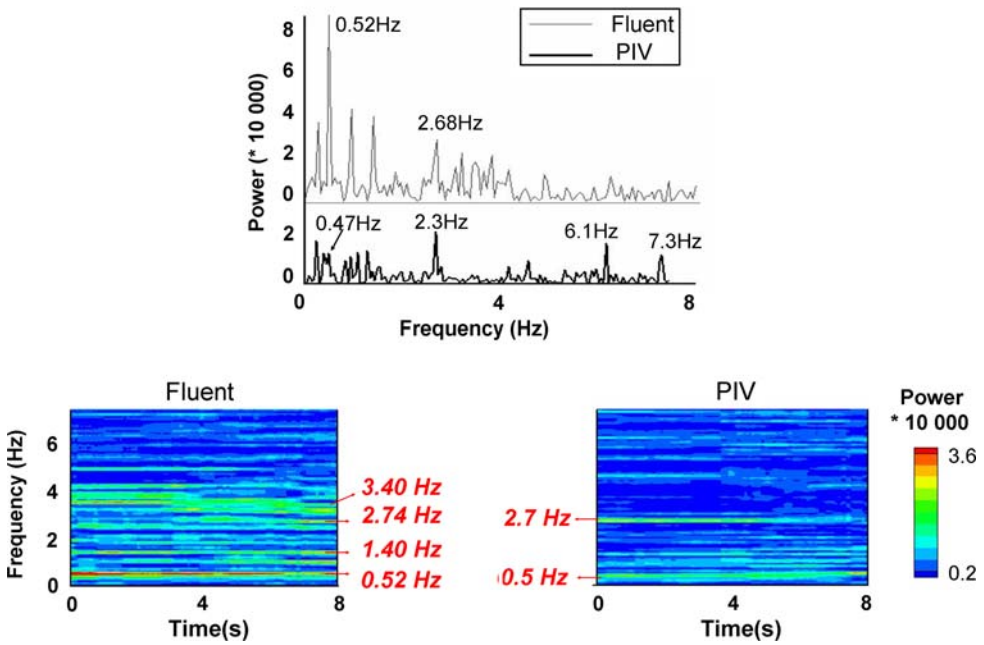

FIGURE 9. (Top) Power spectrum of instantaneous velocity time series sown in Fig. 6. (Bottom) Carpet plots of the power spectrum obtained for the same time series using a moving time window of 10 s.

longer showed intertwined frequencies, with fast oscillations embedded in a slower periodic motion. On the contrary most of the energy was contained in lower frequencies (typically 1.4 and 2.2 HZ for 3 and 4 L/min, respectively).

Model B: Analysis of Unstable Vortex Structures

The above-mentioned time series suggest that different scales of flow motion come into play and interact with each other. This can be readily illustrated when looking into the dominant vortices associated with different flow conditions, as is shown in Figs. 11–13 for the two extreme flow flow-splits (70/30 and 30/70 LPA/RPA) at 4 L/min. In this series of figures, coherent 3D vortex cores are visualized by plotting the second invariant of the deformation matrix, Q iso-surfaces.

At 30/70 LPA/RPA (Fig. 11), a precise repetition of flow structures can be observed with a distinct period of fluctuation, which is also apparent in the power spectrum plots (Fig. 10). At this split, five distinct structures coexist (see Fig. 11). Two of them (g1 and g2) persist in time, while other structures (s1, s2, s3) are periodically formed and swept away from the flow domain. The flow field alternates between the two states (a/c and b) plotted in Fig. 11. The alternating vortex cores s1 and s2 shed from the IVC/RPA and SVC/LPA anastomoses, respectively. The last alternating structure (s3) is believed to occur due to the interaction of persistent coherent structure pair (g1 and g2).

At 70/30 LPA/RPA on the other hand, the flow behaves in a seemingly chaotic manner (Fig. 12) and no periodic flow pattern can be distinguished. This flow regime is similar to what was observed in Model A at all flow regimes with numerous flow states and structures leading to the jagged power spectrum plots shown in both Figs. 9 and 10e. Despite the fact that there were no exact repetitive phenomena, three main flow events could still be identified that grossly governed the flow structure in the connection (see Fig. 12):

- formation of crescent-shaped SVC vortices (c1 and c2),
- complex fingering (f1 through f4) of the main LPA vortex core (m),
- and shedding (r) of these fingers into the RPA branch.

Figure 12a illustrates the crescent SVC vortex (c1) that originates from the posterior LPA/SVC anastomosis edge, and slightly extends into the connection towards the anterior direction. At this time, the main LPA vortex core (m) enlarges in size at the connection region center with emerging protrusions that swirl over each other (s). An abrupt IVC diameter increase at the IVC anastomosis creates two minor temporary vertical

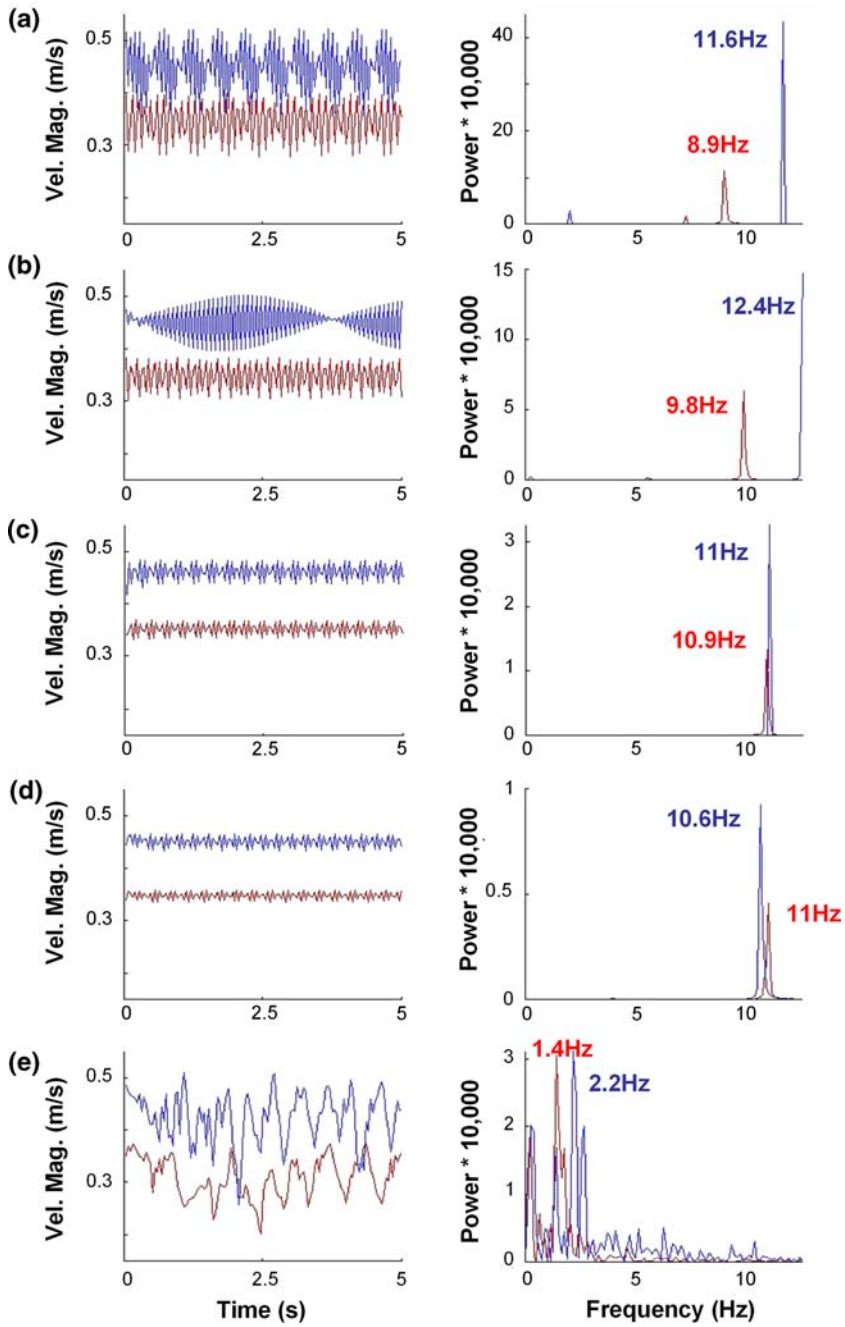

FIGURE 10. Time series of instantaneous velocity magnitude and corresponding power spectrums in the connection region of Model B for different LPA/RPA splits and total cardiac outputs. (a) 30/70; (b) 40/60; (c) 50/50; (d) 60/40; (e) 70/30. Blue: 4 L/min, Red: 3 L/min.

structures (v1 and v2). In Figs. 12b and 12c, the main LPA vortex core extends into the RPA, forming finger-like structures (f1, f2 and then f2a, f2b). The crescent-shaped SVC vortex (c1) curves down towards the IVC and terminates at the posterior wall, now spanning the entire connection diagonally. At this convenient location, it starts to interact with the main LPA vortex core (m). While its starting point remains anchored (p), the crescent vortex orients itself in the anterior-posterior direction and manages to combine with the f1 finger (Fig. 12d). This configuration being relatively instable disintegrates into pieces (Fig. 12e), leaving many irregular-shaped small-scale structures. Additionally the LPA core extends deeper into the RPA, now

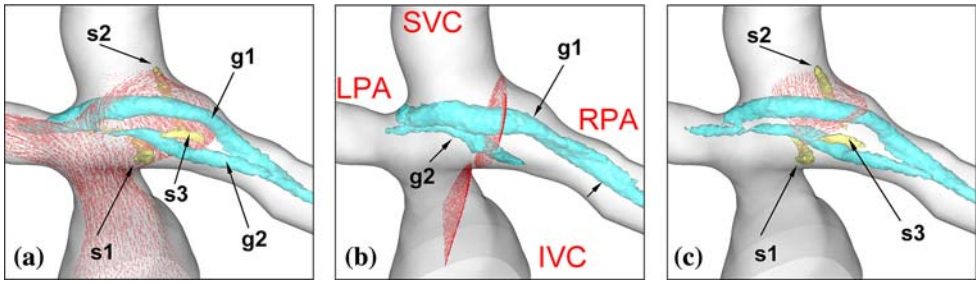

FIGURE 11. Unsteady flow topology of Model B at 30/70 LPA/RPA visualized by the second invariant of the deformation tensor (q = 20,000). Time difference between each snapshot is 0.04 s. The three snapshot depict an entire periodic cycle, with (a) and (c) corresponding to the same state. The different states of the flow structure are defined by the two permanent tubular structures (g1 and g2, in blue in the figures) running from LPA to RPA, which coexist with the oscillating anterior-posterior vortex cores (s1, s2 and s3, in yellow in the figure). The red arrows illustrate the velocity vectors along various sliced planes.

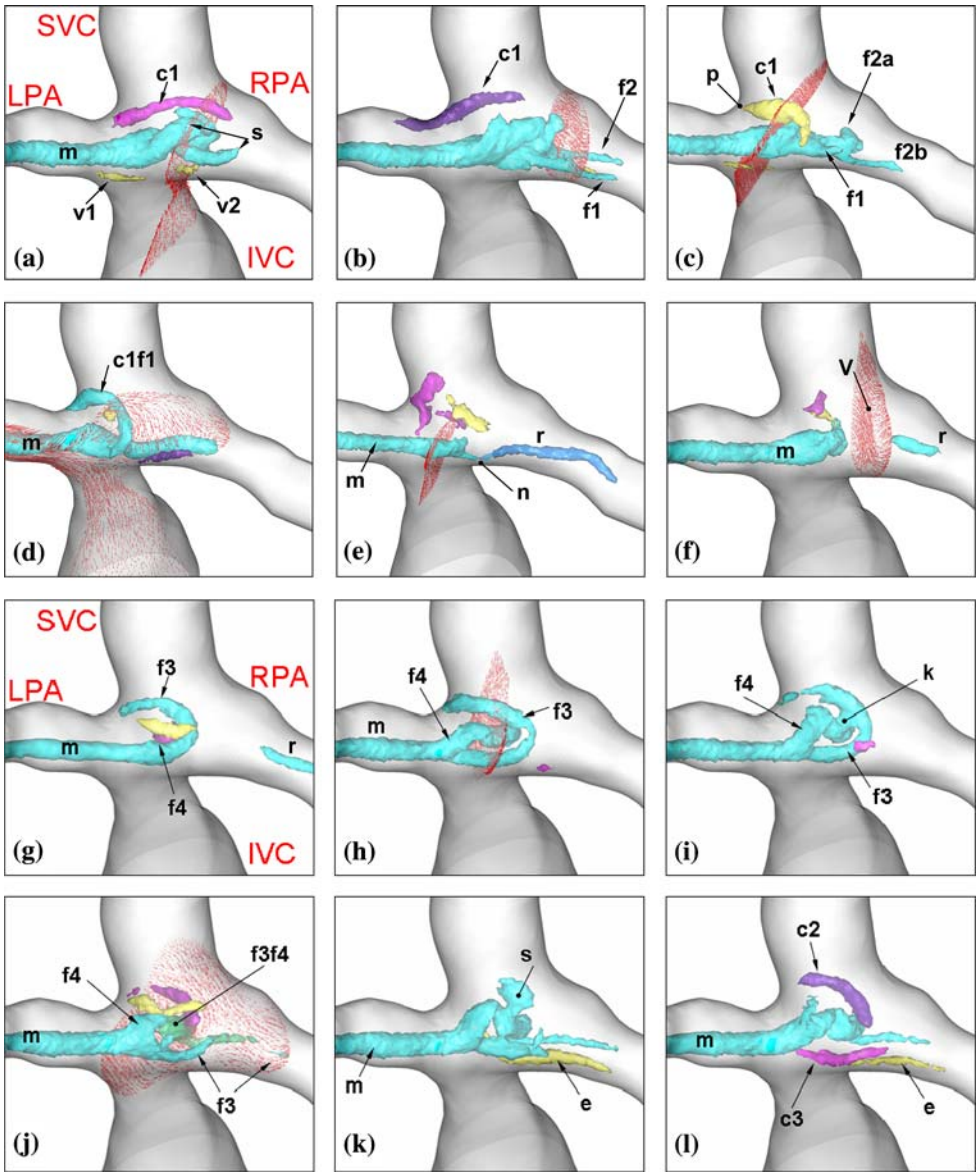

FIGURE 12. Unsteady flow topology of Model B at 4L/min, 70/30 LPA/RPA visualized by the second invariant of the deformation tensor (q = 13,000). Individual vortex cores are plotted with different colors. Time difference between each snapshot is 0.04 s. Details on the topology and nomenclature of these flow structures are provided in Section ''Model B: Analysis of Unstable Vortex Structures.'' The red arrows show the velocity vectors along various sliced planes.

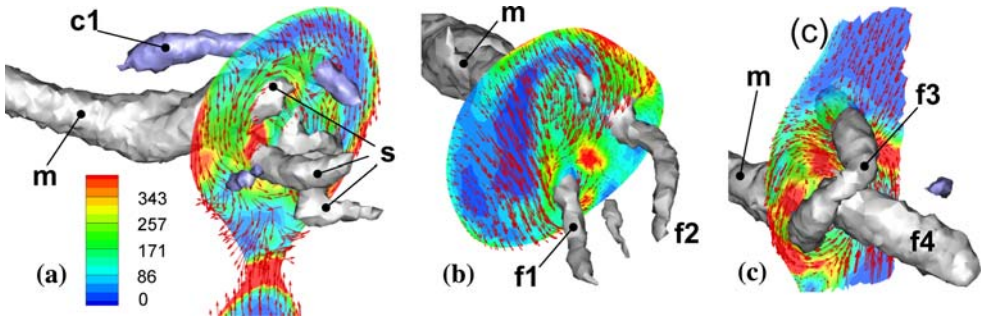

FIGURE 13. Dissipation function (power loss, in mW) plotted along selected slices during the "fingering" events for Model B at 4L/min, 30/70 LPA/RPA flow split condition (see Fig. 12). Power loss hot spots coincide with the counter-rotating vortices. The three instants in time depicted in (a), (b) and (c) correspond to the ones depicted in Figs. 12a, 12b and 12h, respectively. Details on the topology and nomenclature of these flow structures are provided in Sections "Model B: Analysis of Unstable Vortex Structures" and "TCPC Dynamics: Relationship between Flow Structures and Power Losses."

forming two elongated tubes (m and r) and starting to neck (n). In Fig. 12f, the vortex tube r finally sheds away. This vortex shedding is most likely due to the interaction between the vortex tubes and the incoming SVC flow (V). At that stage (from Figs. 12h–12k), the main vortex core (m) undergoes series of complex configuration changes, generating new and highly curved fingers (f3 and f4), which interact and ultimately form a large structure at the center of the SVC (s), (Fig. 12k). This large vortex core (s) starts to break up leading to the formation of crescent-shaped structures at the SVC and IVC anastomosis (c2 and c3, respectively), (Fig. 12l). This configuration marks the beginning of a new cycle, even though not exactly identical to the one depicted in Fig. 12a.

The described series of events for the 70/30 LPA/RPA flow setting in Model B starts from a local maximum power loss point (Fig. 12a) (2.471 mW) and gradually decreases to a local minimum (Fig. 12e) (2.218 mW) configuration and ends in another local maximum (Fig. 12k) (2.419 mW). This trend implies that high global power loss values coincide with the finger formation events and SVC vortex dwindle. Hot spots in power loss contours (Fig. 13) are observed to coincide with the shear zones generated by the temporary counter-rotating structures and complex fingering events. In addition to the boundary layers, which are always highly dissipative, flow regions squeezed between two vortex cores also contribute significantly to the internal hydrodynamic power loss, (Fig. 13c).

DISCUSSION

This study presented a new attempt to better model TCPC hemodynamics using improved meshing and simulation options offered by the commercially available CFD package FLUENT. The purpose of this study was 2-fold: (1) assess the strength and limitations of the CFD package retained for the study (Sections "Mesh Generation" to "CFD Validation: Time-Averaged Flow Fields"), and (2) compare the unsteady flow features of two different TCPC templates (Sections "CFD Validation: Unsteady Flow Features" and "TCPC Dynamics: Intra-Atrial vs. IVC-to-MPA").

Mesh Generation

A major challenge in the numerical simulation of blood flow in realistic cardiovascular anatomies stems from the arbitrary geometrical complexity of the *in vivo* sytems. By complexity, we are referring to the multiply curved nature of the boundaries as well as the possibility of multiple inlets and outlets. These factors require extra meshing effort to accurately resolve the geometric details of the boundary and associated flow patterns. Meanwhile, the issue of complexity must be balanced against the need to optimize the mesh size, thus minimizing solver-time and memory requirements.

In terms of computational efficiency and global accuracy, a structured grid made up of hexahedral elements is the most desired approach. The benefits of such a grid include the ability to align the hexahedral elements with the predominant flow direction and the reduction in solution time that is gained when adhering to strict rules on element ordering. Software tools are available for creating such meshes, but typically require a significant level of user interaction—ranging from an hour to a day or even days, depending on the geometry and the users level of experience. Unstructured grids consisting of tetrahedral elements are a more practical choice for flows with complex geometries because they more readily adapt to the wall geometry. Meshes consisting of entirely tetrahedral elements are already being employed in complex anatomical domains with great success.[19,20,25] And for

simpler anatomies, hexahedral unstructured grids can be readily implemented[14] as the boundary-layer mesh uniformity can be controlled with reasonable manual mesh generation effort. The algorithms for creating unstructured grids are also more amenable to automation. The benefits of automation being that one can conduct virtual clinical trials or test hypotheses on a large patient population with minimal user intervention.

In the present work, we used the Hex Core grid generation approach in GAMBIT to create a mesh consisting of an internal core of *uniform hexagonal cube mesh elements* surrounded by transition layers of tetrahedral elements. After a series of standard tests, this scheme was found to provide the best domain discretization for FLUENT. Final mesh numbers and densities utilized for both anatomical models (Table 1) were comparable to the finest mesh sizes that have been used in our previous (steady-state) studies.[22,23,32] The Hex Core meshes were generated in approximately 1 h. This time is similar to that required to generate an unstructured tetrahedral mesh layout, but has the added benefit of containing a core of equally sized hexahedral (brick) elements that covers ~80% of the computational domain. Convergence of the Hex Core layout was also considerably faster than that of the tetrahedral mesh layout. Variations on the details of the Hex Core mesh architecture (like interface size, interface grading, tet orientation) can improve the convergence and quality even further but was not investigated in this study. The values retained for this study were selected based on previous experience.

CFD Validation: Time-Averaged Flow Fields

Model A was retained as the validation test-case because our experimental *in vitro* observations revealed higher degrees of unsteadiness and flow complexity in Model A versus Model B. The performance of the meshing methodology and FLUENT settings used in this study were compared to those of an earlier study using another commercially available CFD code, FIDAP. The accuracy of the flow simulations conducted for this study was assessed at two different levels: first by comparing the experimental and numerical time-averaged flow fields, and then looking into the transient unsteady flow features.

The time-averaged flow fields obtained with the two flow solvers captured the bulk flow features with reasonable accuracy. However, when looking at the flow structure in more detail, the transient flow studies were in better agreement with experimental observations. The relatively larger numerical errors in the lower order flow solution obtained from FIDAP are likely due to the smeared velocity gradients present in the localized flow motion. The computational accuracy achieved by the current study can be attributed to the high-order approximation of the nonlinear convective terms and management of unsteady derivatives in the momentum equation. As shown in Fig. 6, the CFD flow profiles in the SVC inflow region (Section A-A) deviated from the experimental measurements despite excellent agreement in other locations (see Section B-B for example). This deviation is attributed to the loss of accuracy in the 2D PIV measurements due to the three-dimensionality of the SVC inflow jet, which dives down into the pouch region almost perpendicularly to the PIV measurement plane. This hypothesis is supported by the fact that the CFD flow profiles integrated over the cross-section matched the experimental mass-flow rate (measured with the rotameters during PIV experiments) within the limits of flow measurement error (10%).

CFD Validation: Unsteady Flow Features

Figure 7 displays a few instantaneous snapshots of the experimental and numerical flow fields. In order for the figures to be more easily readable, not all of the flow vectors are represented. Apart from a few outliers, which may be noticed in the experimental flow fields and are due to the unavoidable noise and laser light reflections, the instantaneous velocity fields obtained with FLUENT were in good qualitative agreement with the PIV data both in terms of velocity magnitude and flow direction.

From a more quantitative point of view, the time-series of instantaneous velocity magnitude obtained with FLUENT in the connection area (Point P in Fig. 5) were in good agreement with the PIV data (see Figs. 8 and 9), especially in the lower frequency range. This agreement is noticeable as in this flow regime the peak frequency was also found to be dynamically changing as illustrated in the carpet plots in Fig. 9. However, such high temporal resolution could not be achieved in other areas like the SVC inflow region (Point I in Fig. 5). For that point, the experimental measurements demonstrated a degree of unsteadiness comparable to what was observed in the pouch region (Point P), while the CFD simulations resulted in steadier flow behavior. A potential source of explanation for this discrepancy could have been the unphysical implementation of the inflow boundary conditions. However, this hypothesis is obviated by the fact that the over-damping of unsteadiness remained even after extending the entrance length to over 30 vessel diameters. A more likely explanation is the relatively coarser grid resolution in the narrow SVC vessel and the close-by wall boundary conditions, which constrained the degrees of freedom for the flow instabilities.

Based on dye visualization experiments, the frequency of the dominant flow oscillations had been estimated to be 11.1 ± 1.25 Hz.[23] However, the major oscillations occur in the region where the SVC inflow collides with the large flow recirculation, close to the SVC anastomosis. As discussed above, the numerical results obtained with FLUENT in that region gave steadier results than what was observed experimentally. No peak was observed at 11.1 Hz in the PIV data either, due to the low sampling rate of our PIV system (sampling frequency: 15 Hz, maximum frequency resolved: 7.5 Hz). Frequencies higher than 7.5 Hz are expected to wrap around, so that 11.1 + 1.25 Hz would in practice correspond to 2.6 + 1.25 Hz with our PIV equipment. Higher frequency energies may thus have contributed to the low frequency peaks observed experimentally.

TCPC Dynamics: Intra-Atrial vs. IVC-to-MPA

The intra-atrial connection (Model A) demonstrated higher degrees of flow unsteadiness than the IVC-to-MPA type connection (Model B), both in the in vitro experiments and in the computations. The IVC-to-MPA connection in Model B resulted in a smoother connection, yielding a smoother and steadier flow field. Similar observations have also been done in an extra-cardiac connection with a synthetic graft.[32] While a large-scale study is still needed to draw any statistically significant conclusion, our findings suggest that pouch type anatomical connections with disproportionate inflow vessels (like the SVC in Model A) and zero caval offset (Model A) favors the type of flow instabilities observed in this study.

Moreover, the antero-posterior offset between the IVC and SVC in the intra-atrial model might also have contributed to the increased flow instability observed for that geometry. In a straight pipe, vorticity will be concentrated along the walls. If the pipe opened into a T-connection, these vortices would shed into the connection yielding unsteady recirculations dictated by the rhythm of the vortex shedding. In Model A, due to a large antero-posterior offset between the venae cavae, the vortices shedding from both IVC and SVC do not directly interact, yielding large recirculation regions and important flow unsteadiness. Instead of generating a large chaotic recirculation region as was observed in Model A, the interaction of the two incoming streams resulted in coherent, periodic flow structures with a vorticity core limited to the RPA-LPA axis.

Flow instabilities increase power losses, but also help mix the hepatic blood with the rest of the systemic venous return, thus yielding a better distribution of the nutrients and growth factors to both lungs. Hence, if a small amount of flow instability may be beneficial, important flow instabilities may be detrimental. Simulations at different cardiac outputs and pulmonary flow splits clearly demonstrate that the levels of unsteadiness and the instability modes can change with the hemodynamic operating point. Extreme pulmonary flow splits and large cardiac outputs seemed to favor flow instabilities.

TCPC Dynamics: Relationship between Flow Structures and Power Losses

The complex unsteady flow structures naturally influence the hydrodynamic power loss in the TCPC. Hydrodynamic power losses for the stable models (or flow conditions) are found to deviate less from the mean power loss value compared to the unstable models. For example, in Model B at 4 L/min, the deviation in overall power loss is ~2% vs. ~6% for the 30/70 and 70/30 LPA/RPA split, respectively (Even a 6% percent change in power loss is considered significant as recent lumped parameter studies[21,32] showed that this can correspond to ~10% acute change in the total cardiac output). Based on this dynamic relationship between control volume power losses and overall flow behavior, power losses may actually be a good candidate for time series and subsequent frequency analysis. Performing a temporal analysis of local quantities such as velocity or vorticity magnitudes is useful for CFD validation purposes, but of limited help for large scale clinical studies as it only provides local flow information and cannot allow for a general and systematic comparison in between TCPC templates.

Limitations and Future Work

This study highlighted the importance of the transient flow dynamics of the TCPC and its impact on the energy dissipation. A few limitations should however be mentioned. First, this study was conducted using steady inflow conditions. This assumption, which is useful in development stages, should ultimately be alleviated to account for intra-thoracic pressure variations due to breathing, diaphragm and heart motion, which are known to induce significant unsteadiness into the otherwise steady single-ventricle venous flow. Changing the inflow conditions to unsteady patient-specific ones will most likely alter the observed flow structures and associated power losses. This will be especially true if the IVC and SVC flow streams are not in phase; in which case, the interaction between the different vortex cores will drastically differ from the steady inflow results. In addition, this study assumes the vessel walls to be rigid, which is expected to augment the predicted flow unsteadiness. Numerical simulations with flexible walls have recently been presented by *Masters et al.*[17,18] for idealized TCPC

geometries, as well as for arterial problems.[3,8,11,26] However, relieving these assumptions in patient-specific geometries will require the development of fast and high-resolution solvers, which is where the commercial flow solver and mesh generation approaches used in this study may come into play.

CONCLUSIONS

This study investigated the applicability of a commercially available flow solver (FLUENT) to the complex, 3-D, and highly unsteady, patient-specific flows observed in Fontan patients. The geometry was meshed using a Tet/Hybrid, Hex-Core grid layout, which provided a high-quality mesh after minimal (< 1 h) user-time. The first model, an intra-atrial geometry with highly unstable flow features, was used for validation purposes and demonstrated good agreement between the experimental and numerical results. Similar agreement in the same geometry has previously been reported by Pekkan *et al.*[23] using an in-house code on structured grids. Achieving the same level of experimental agreement and accuracy now with an *unstructured* grid will enable fast transient patient-specific hemodynamic analysis within the realm of practical time steps and encourages its clinical utilization in studies involving large number of anatomical models.

The second arm of this study was to apply the validated methodology to a second TCPC morphology, investigating further the flow features associated with different TCPC anatomies, namely an intra-atrial connection and an IVC-to-MPA connection. This study revealed higher degrees of flow instabilities in the intra-atrial connection, which may be attributed to the bulging intra-atrial baffle. The severity of the intrinsic flow instabilities also showed a strong dependence upon the operating flow conditions, namely on the total cardiac output and pulmonary flow split.

ACKNOWLEDGMENTS

This work was supported by a grant from the National Heart, Lung, and Blood Institute, HL67622. We also acknowledge Dr. Dave Frakes and Mr. Hiroumi Kitajima for processing the patient MRI datasets. The glycerin for the experimental work was provided by P&G, Cincinnati, OH.

REFERENCES

[1]Baran, O. U. Control methodologies in unstructured hexahedral grid generation, PhD Thesis, Vrije Universteit Brussel, November 2005.

[2]Barton, I. E. Comparison of simple- and piso-type algorithms for transient flows. *Int. J. Numer. Methods Fluids* 26:459–483, 1998.

[3]Bathe, M., and K. D. Kamm. A fluid-structure interaction finite element analysis of pulsatile blood flow through a compliant stenotic artery. *J. Biomech. Eng.* 121(4):361–369, 1999.

[4]Cebral, J. R., M. A. Castro, S. Appanaboyina, C. M. Putman, D. Millan, and A. F. Frangi. Efficient pipeline for image-based patient-specific analysis of cerebral aneurysm hemodynamics: technique and sensitivity. *IEEE Trans. Med. Imaging*. 24(4):457–467, 2005.

[5]Cebral, J. R., M. A. Castro, J. E. Burgess, R. S. Pergolizzi, M. J. Sheridan, and C. M. Putman. Characterization of cerebral aneurysms for assessing risk of rupture by using patient-specific computational hemodynamics models. *Am. J. Neuroradiol.* 26(10):2550–2559, 2005.

[6]Dasi, L., K. Pekkan, K. Whitehead, M. Fogel, and A. P. Yoganathan. Hepatic blood flow distribution in the total cavopulmonary connection: patient-specific anatomical models. In: Proceedings of the ASME 2007 Summer Bioengineering Conference (SBC2007), Keystone Resort & Conference Center, Keystone, Colorado, June 20–24, 2007.

[7]DeGroff, C., B. Birnbaum, R. Shandas, W. Orlando, and J. Hertzberg. Computational simulations of the total cavopulmonary connection: insights in optimizing numerical solutions. *Med. Eng. Phys.* 27(2):135–146, 2005.

[8]Di Martino, E. S., G. Guadagni, A. Fumero, G. Ballerini, R. Spirito, P. Biglioli, and A. Redaelli. Fluid-structure interaction within realistic three-dimensional models of the aneurysmatic aorta as a guidance to assess the risk of rupture of the aneurysm. *Med. Eng. Phys.* 23(9):647–655, 2001.

[9]Dong, S., G. M. Karniadakis, and N. T. Karonis. Cross-site computations on the Tera-Grid. *Comput. Sci. Eng.* 7(5):14–23, 2005.

[10]Ensley, A. E., P. Lynch, G. P. Chatzimavroudis, C. Lucas, S. Sharma, and A. P. Yoganathan. Toward designing the optimal total cavopulmonary connection: an *in vitro* study. *Ann. Thorac. Surg.* 68:1384–1390, 1999.

[11]Figueroa, A. C., I. E. Vignon-Clementel, K. E. Jansen, T. J. R. Hughes, and C. A. Taylor. A coupled momentum method for modeling blood flow in three-dimensional deformable arteries. *Comput. Methods Appl. Mech. Eng.* 195:5685–5706, 2006.

[12]Fischer, P., F. Loth, S.-W. Lee, D. Smith, H. Tufo, and H. Bassiouny. Parallel simulation of high Reynolds number vascular flows. In: Proc. of Parallel CFD, 2005.

[13]Freitas, C. J. Perspective: selected benchmarks from commercial CFD codes. *J. Fluids Eng.* 117(2):208–218, 1995.

[14]Hunter, K. S., J. Craig, C. J. Lanning, S. Y. J. Chen, Y Zhang, R. Garg, D. D. Ivy, and R. Shandas. Simulations of congenital septal defect closure and reactivity testing in patient specific models of the pediatric pulmonary vasculature: a 3D numerical study with fluid-structure interaction. *J. Biomech. Eng.* 128(4):564–572, 2006.

[15]Khunatorn, K., B. Shandas, C. DeGroff, and S. Mahalingham. Comparison of *in vitro* velocity measurements in a scaled total cavopulmonary connection with computational predictions. *Ann. Biomed. Eng.* 31(7):810–822, 2003.

[16]de Leval, M. R. The Fontan circulation: a challenge to William Harvey? *Nat. Clin. Pract. Cardiovasc. Med.* 2(4):202–208, 2005.

[17]Masters, J. C., M. Ketner, M. S. Bleiweis, M. Mill, A. Yoganathan, and C. L. Lucas. The effect of incorporating

vessel compliance in a computational model of blood flow in a total cavopulmonary connection (TCPC) with caval centerline offset. *J. Biomech. Eng.* 126(6):709–713, 2004.

[18]Masters, J. C., M. Ketner, M. Mill, A. P. Yoganathan, and C. L. Lucas. Assessing the effect of compliance on the efficacy of the total cavopulmonary connection. *J. Biomech. Eng.* 2006 (in press).

[19]Migliavacca, F., R. Balossino, G. Pennati, G. Dubini, T. Y. Hsia, M. R. de Leval, and E. L. Bove. Multiscale modelling in biofluidynamics: application to reconstructive pediatric cardiac surgery. *J Biomech.* 39(6):1010–1020, 2006.

[20]Moyle, K. R., L. Antiga, and D. A. Steinman. Inlet conditions for image-based CFD models of the carotid bifurcation: is it reasonable to assume fully developed flow? *J. Biomech. Eng.* 128(3):371–379, 2006.

[21]Pekkan, K., D. Frakes, D. Zélicourt, C. W. Lucas, W. J. Parks, and A. P. Yoganathan. Coupling pediatric ventricle assist devices to the Fontan circulation; simulations with a lumped parameter model. *ASAIO J.* 51(5):618–628, 2005.

[22]Pekkan, K., H. Kitajima, J. Forbess, M. Fogel, K. Kanter, J. M. Parks, S. Sharma, and A. P. Yoganathan. Total cavopulmonary connection flow with functional left pulmonary artery stenosis—fenestration and angioplasty *in vitro*. *Circulation* 112(21):3264–3271, 2005.

[23]Pekkan, K., D. de Zélicourt, L. Ge, F. Sotiropoulos, D. Frakes, M. A. Fogel, and A. P. Yoganathan. Physics-driven CFD modeling of complex anatomical cardiovascular flows-a TCPC case study. *Ann. Biomed. Eng.* 33(3):284–300, 2005.

[24]Perot, B. Conservation properties of unstructured staggered mesh schemes. *J. Comput. Phys.* 159(1):58–59, 2000.

[25]Tang, B. T., C. P. Cheng, M. T. Draney, N. M. Wilson, P. S. Tsao, R. J. Herfkens, and C. A. Taylor. Abdominal aortic hemodynamics in young healthy adults at rest and during lower limb exercise: quantification using image-based computer modeling. *Am. J. Physiol. Heart. Circ. Physiol.* 291(2):H668–H676, 2006.

[26]Tezduyar, T. E., S. Sathe, T. Cragin, B. Nanna, B. S. Conklin, J. Pusewang, and M. Schwaab. Modelling of fluid–structure interactions with the space–time finite elements: arterial fluid mechanics. *Int. J. Numer. Meth. Fluids* 54(6–8):901–922, 2007.

[27]Whitehead, K. K., K. Pekkan, R. Doddasomayajula, H. D. Kitajima, K. S. Sundareswaran, A. P. Yoganathan, and M. A. Fogel. Extracardiac Fontan demonstrates lower power loss compared to intracardiac Fontan—a computational fluid dynamics study. Presented at the Annual Scientific Sessions of the American College of Cardiology, March 24–27, 2007.

[28]Yerneni, V., K. Pekkan, P. Nourparvar, D. de Zélicourt, J. Rossignac, L. Dasi, F. Sotirpoulos, and A. P. Yoganathan. Comparative CFD study of hemi-Fontan and Glenn anastomosis: idealized and anatomical models with free-form deformed variations. In: Proceedings of ASME-Bio2006 Summer Bioengineering Conference, Florida, June 21–25, 2006.

[29]Yue, X., F. N. Hwang, R. Shandas, and X. C. Cai. Simulation of branching blood flows on parallel computers. *Biomed. Sci. Instrum.* 40:325–330, 2004.

[30]Zhang, X., D. Schimdt, and B. Perot. Accuracy and conservation properties of a three-dimensional unstructured staggered mesh scheme for fluid dynamics. *J. Comput. Phys.* 175(2):764–791, 2002.

[31]de Zélicourt, D., K. Pekkan, H. Kitajima, D. Frakes, and A. P. Yoganathan. Single-step stereolithography of complex anatomical models for optical flow measurements. *J. Biomech. Eng.* 127(1):204–207, 2005.

[32]de Zélicourt, D., K. Pekkan, W. J. Parks, K. Kanter, M. Fogel, and A. P. Yoganathan. Flow study of an extracardiac connection with persistent left superior vena cava. *J. Thorac. Cardiovasc. Surg.* 31(4):785–791, 2006.